Toward Scalable High Performance Lithium-Metal Anodes: Hierarchical Self-Grown Carbon-Metal Nanofiber Scaffolds

Xinhua Liu,[1,2] Xiaojuan Qian,[3] Weiqiang Tang,[4] Yang Hua,[1] Hui Luo,[2] Yan Zhao,[2] Rui Tan,[2] Mo Qiao,[2] Huizhi Wang,[2] Shuangliang Zhao,[4] Chao Lai,[3] Magda Titirici,[2] Nigel P. Brandon,[2] Shichun Yang,[1,*] and Billy Wu[2]

[1]School of Transportation Science and Engineering, Beihang University, 100191, Beijing, P. R. China
[2]Imperial College London, Sough Kensington Campus, SW7 2AZ, London, UK
[3]School of Chemistry and Materials Chemistry, Jiangsu Normal University, 221116, Jiangsu, P. R. China
[4]State Key Laboratory of Chemical Engineering and School of Chemical Engineering, East China University of Science and Technology, 200237, Shanghai, China

Lithium metal anodes are of great interest for advanced high energy density battery systems such as lithium-air, lithium-sulfur and solid state batteries, due to their low electrode potential and ultra-high theoretical capacity. There are, however, several challenges limiting their practical applications, which include low Coulombic efficiency, the uncontrollable growth of lithium dendrites and poor rate capability. Here, a rational design of 3D structured lithium metal anodes comprising *in-situ* growth of cobalt-decorated nitrogen-doped carbon nanotubes on continuous carbon nanofibers is demonstrated via electrospinning. The porous and free-standing scaffold can enhance the tolerance to the stresses caused by the intrinsic volume change during Li plating/striping, delivering a significant boost in both charging/discharging rates and stable cycling performance. Characterization and density functional theory calculations show that the conductive and uniformly distributed cobalt-decorated carbon nanotubes can effectively reduce the local current density and more easily absorb Li atoms, leading to more uniform Li nucleation during plating. The present work thus presents an advance on scalable and cost-effective strategies for novel electrode materials with 3D hierarchical microstructures and mechanical flexibility for lithium metal anodes.

Given the urgent need to reduce greenhouse gas emissions from road transport, lithium-ion batteries (LIB) have now transitioned from applications in portable electronics to electric vehicles (EV). However, improvements in energy/power density, cost reduction and lifetime are still required. Lithium (Li) metal anodes have long been considered as the "Holy Grail" battery chemistry with regards to next generation energy-storage systems due to its ultra-high theoretical specific capacity (3860 mA h g^{-1}), the lowest reduction potential (−3.04 V vs the standard hydrogen electrode), and very low density (0.534 g cm^{-3}).[1–3] However, Li metal electrodes suffer from poor lifetime, low rate capability and safety issues which limits their more widespread uptake.

The causes of these problems are mainly due to the high reactivity of Li metal toward the electrolyte and non-uniform reaction current densities over the electrode surface.[1] Freshly deposited Li metal shows a high reactivity towards most organic electrolytes leading to unstable solid electrolyte interphase (SEI) formation and growth. When cycled, isolated regions of Li can also be formed which further deteriorates the Coulombic efficiency.[4] The conventional electrode of Li on a Cu current collector suffers from Li dendrites problem because of the heterogeneous charge distribution, which gets worse as the dendrites grow due to further intensification of the non-uniform reaction current density.

Over the past several years, tremendous amounts of research have been devoted to develop Li metal anodes which can tolerate the huge volume changes, inhibit dendrite growth and ways of constructing stable and uniform SEI layers on the Li anode. These Li dendrites can be supressed, and the Coulombic efficiency can be improved, by proper designs of the SEI, optimizing the electrolyte contents, separators/artificial protective layers,[5–7] engineering solid electrolytes[8–10] and employing

an artificial SEI coatings on the anode to name but a few promising strategies.[11,12] However, despite the encouraging achievements towards constructing stable SEI layers, the nature of Li dendrite growth arising from heterogeneous Li reaction current density and the electrode volume variation problems on conventional planar Li foil/Cu surfaces remain a big challenge. As an alternative, 3D structural scaffolds for Li metal anodes are attractive as these can mitigate the bulk volume variations and improve the overall performances during Li plating/stripping due to their stable conductive frameworks for electron transfer and pore structures which enable effective ion transfer.

Anode materials with porous micro or nanostructures have been shown to achieve high electrochemical performance because their enhanced specific surface area can reduce the local current density and make the Li deposition/stripping more uniform. However, the principles around the rational design of these 3D porous architectures are limited. Recently, Zhang et. al.[13] proposed fundamental understanding around the electron and ion transfer factors behind the Li dendrite growth behaviour by employing a phase field model to quantitatively describe the dendrite formation on various conductive structured lithium anodes. In the initial kinetically dominated process, the surface area linearly determines the electroplating reaction rate which is mainly limited by electron transfer in the anode. However, too high a surface area can results in pore blockage leading to reduced plating/stripping kinetics and thus an inversely proportional relationship between reaction rate and surface area due to limited ion transfer in the electrolyte. Therefore, the optimal anode design should combine the following requirements to ensure high current density and long-term cycling performance: 1) dendrite-free morphology with a high surface area conductive framework to reduce local current density; 2) decreased electronic overpotentional through the use of highly conductive materials; 3) maintaining an open pore structure to ensure a stable electrode volume during cycling whilst maintaining interconnected pores to allow for mass transport throughout the electrode[14]; 4) more uniform nucleation of Li by addition of functional groups with strong Li interactions;[15] 5) scalable manufacturing to produce anode materials with applicability in real world systems.

Most proposed Li metal anode materials mainly focused on 3D scaffold designs using graphene, carbon fibre,[16] natural diatomite[17] and metal-based porous hosts with nano-engineered architectures. As a typical example, the channel-like structure of a carbonized eggplant exhibits an interconnected conductive framework and can be a stable "host" for Li metal melt infusion.[2] Furthermore, Xue et. al.[18] developed a hierarchical 3D host by assembling AgNW and graphene into an optimised binary network structure, which can work smoothly at an ultra-high current density of 40 mA cm^{-2} over 1000 plating/stripping cycles with a low overpotential (<120 mV) in symmetric cells. Nitrogen-doped 3D flexible graphitic foams can be employed as a lightweight current collector to realize uniform Li nucleation/growth.[19] Although theoretical calculations have highlighted the beneficial doping effects of nitrogen on carbon for more uniform Li nucleation, only limited literatures show the strong interaction between Li atoms and the functional groups of nitrogen (N)[13,19–21] and oxygen (O)[22] or metal doping. However, the Li metal anodes reported do not fully satisfy all of mentioned design requirements.

Inspired by all aforementioned considerations, we herein present a scalable fabrication route for a rationally designed Li metal scaffold material which consists of Co nanoparticles encapsulated in nitrogen-doped (N-doped) carbon nanotubes (CNTs) which are grown in larger continuous carbon nanofibers. This is achieved through a low cost electrospinning process followed by an easy stabilization and carbonisation process. Firstly, a precursor solution containing 0.6 g Cobalt (II) acetylacetonate ($Co(acac)_2$), 0.6 g of polyacrylonitrile (PAN) and 6 ml N,N-dimethylformamide (DMF) was obtained after magnetic stirring at 55 °C for 24 h. A purple coloured nanofiber film (Figure 1a) was produced via electrospinning by applying 13.5 kV. Subsequently, the electrospun nanofibers were stabilized at 290 °C in air for 2 h with a ramp rate of 2 °C min^{-1} (Figure 1b). Finally, the fully post carbonisation was done in N_2, using a dwell time of 2 h at 300 °C with an initial ramp rate of 2 °C min^{-1} and dwell time 2 h at 850 °C with ramp rate of 5 °C min^{-1}. Figure 1c shows the carbon nanofiber morphology after heat treatment at 550 °C for 2 h, highlighting the exsolved Co nanoparticles on the surface of the carbon nanofibres. At temperatures above 600 °C, these exsolved catalyst nanoparticles begin to grow carbon nanotubes, or "hairs", which were randomly distributed on the surface of the electrospun fibres (Figure 1d). The thermogravimetric trace analysis (TGA)

(Figure S1) shows the rapid decomposition of $Co(acac)_2$ after 200 °C while the slight mass loss below 200 °C is mainly because of the loss of absorbed free and bounded water. Thus, the fibers exhibit a dark colour attributed to the CoO after the stabilisation process.[23] The CoO can be self-assembled and reduced to metallic Co *in-situ* by the heat treatment process. The CNTs form due to the carbon containing decomposition by-products of the PAN during heat treatment which are then catalysed on the Co surface to form the CNTs. The preparation process of the hairy fibres is schematically illustrated in Figure 1. During the synthetic procedure, PAN acts as not only the phase for the formation of fibrous continuous structure, but also the nitrogen and carbon sources for the hairy fiber production via a one-step preparation method without conventional costly and complex steps such as: catalyst deposition, catalyst activation and the additional carbon sources.

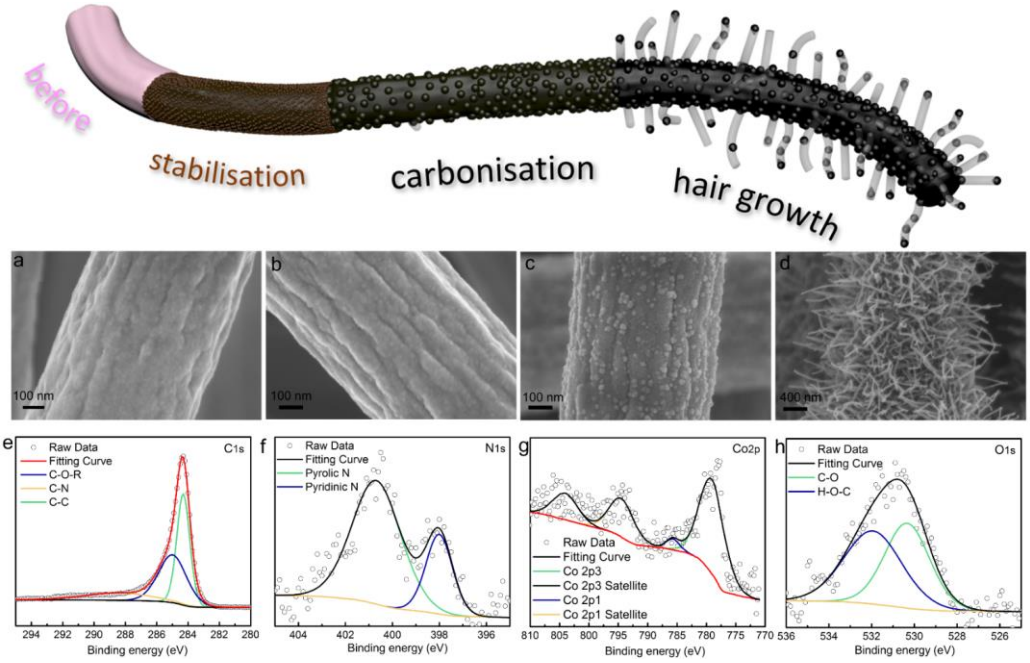

Figure 1. Proposed preparation mechanism for the growth of carbon nanotube on electrospun fibres. (a) The electrospun $Co(acac)_2$ based PAN nanofiber before carbonisation. (b) carbon nanofiber after pre-carbonisation (c) carbon nanofiber after heat treatment at 550 °C for 2 h. (d) carbon nanofiber after post carbonisation at 850 °C. XPS spectra of obtained Co50 HCNF (e) C 1s region, (f) N 1s region, (g) Co 2p region and (h) O1s region.

Figure S2 presents the SEM images of the Co40 and Co50 hairy carbon nanofibers (Co40, postcarbonised from electrospun nanofiber with 40 wt% $Co(acac)_2$; Co50, postcarbonised from electrospun nanofiber with 50 wt% $Co(acac)_2$). The Co50 sample has more hairs than the Co40 because of the increased concentration of $Co(acac)_2$, resulting in more catalyst nanoparticles. The higher magnification SEM images show a diversity of hairy morphologies, with some showing nanoparticles on the tip and some with a unique peapod like CNT structure, however more tip-growth CNTs are observed. The transmission electron microscopy (TEM) images in Figure 2 give information about the morphology of the as-prepared Co50@CNFs and the elemental composition. These Co based CNT-hairs have an approximately average outer diameter of ≈10-20 nm which are upto several hundred nanometers in length (**Figure 2**a and Figure 2b). The wall thickness of the CNTs is between 2 – 7 nm, and consists of ≈5 – 20 (002) graphene layers as observed from the high-resolution TEM (HRTEM) images in Figure 2c. The lattice spacing of the Co nanoparticle was found to be 0.205 nm, which corresponds to the (111) crystal plane in the cubic Co structure.[24] The pure metallic phase of Co can also be identified from energy disperse spectroscopy (EDS) maps, as seen in Figures 2e-i, which show that the detected Co signal is mainly from the Co nanoparticles, whereas the

oxygen signal is highly dispersed, indicating that the Co nanoparticles inside the tubular structure of multi-walled CNTs contains only Co atoms. The X-ray diffraction (XRD) patterns are shown in Figure S3, broad peaks can be found at ≈25° which is linked to the (002) interlayer distance of graphitic carbon. The calculated crystallite sizes for the Co metallic phases were found to be approximately 30 nm. The X-ray photoelectron spectroscopy (XPS) profiles performed on the Co40 and Co50 based samples (Figures 1e-1h and Figure S4) confirms the metallic nature of the nanoparticles from the Co2p spectrum and the functional groups of nitrogen and oxygen are confirmed from C1s and O1s spectrums. As shown in Figure 1f, the XPS N1s spectrum can be de-convoluted into peaks of pyridinic nitrogen (N-6, ≈398.0 eV) and pyrrolic nitrogen (N-5, ≈400.7 eV). According to literatures, the functional groups of nitrogen (N)[13,19–21] and oxygen (O)[22] can provide beneficial doping effects for more uniform Li nucleation. Therefore, these 3D free standing hairy carbon nanofibers (HCNFs) can be used as effective and conductive Li deposition scaffolds for Li metal anode batteries.

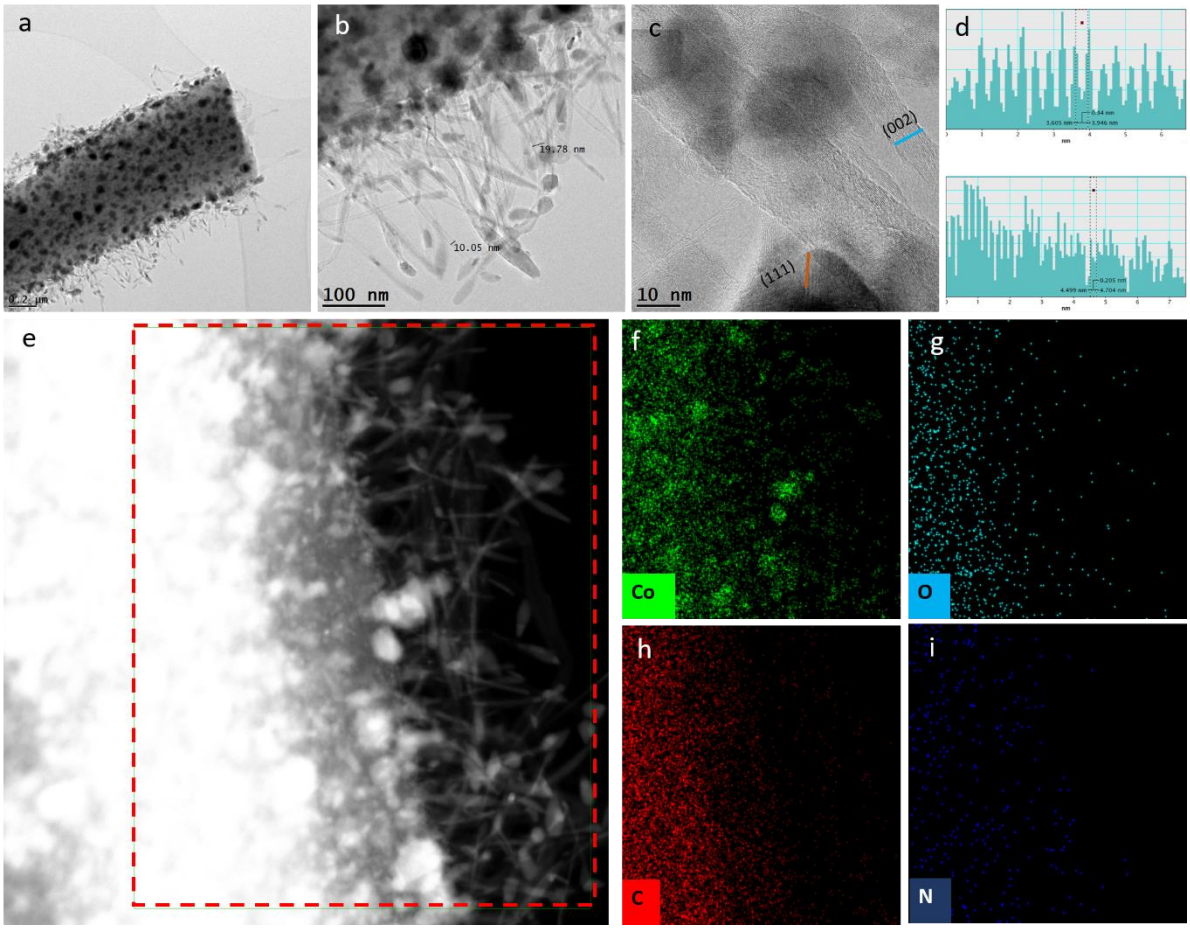

Figure 2. (a,b)TEM images of the morphology of Co50@CNFs samples; (c) HRTEM image of the Co based nanotubes-hairs; (d) lattice profile of CNTs (blue) and cubic Co (orange); (e-i) HAADF STEM image and EDS mapping.

Following microscopic and spectroscopic investigation, the metallic Li nucleation and growth behaviours on Co50 HCNFs were investigated under various current densities from 1 mA cm^{-2} to 8 mA cm^{-2}. The SEM images of their cross-sections and surfaces with initial Li plating are shown in Figure 3. With the low-loading (i.e., 1 mAh cm^{-2} in Figures 3b and 3c), the morphology of the Co50 HCNF shows uniform deposition on the hierarchical structures, a smooth surface, a 3D interconnected continuous network and plenty of void space for ionic

transport. When the Li loading was increased to 2 mAh cm^{-2} (Figures 3e and 3f), 4 mAh cm^{-2} (Figures 3h and 3i) and 6 mAh cm^{-2} (Figures 3k and 3l), the HCNFs can still maintain uniform Li distribution, with no recognizable Li dendrite formation. Although a slight rough plating can be observed at a high loading of 8 mAh cm^{-2} (Figures 3n and 3o), there are still pores for Li deposition and ionic transport. From their cross-sectional SEM images (Figures 3a, 3d, 3g, 3j and 3m), the Co50 HCNF can maintain a relatively constant electrode thickness from 52 µm to 62 µm with various current Li deposition. The high mechanical strength and interconnected porous conductive structure can effectively facilitate the volume change during Li plating. The Co50 HCNF electrode also has a high electrical conductivity of 227.6 $S.m^{-1}$ (Figure S5), therefore, such 3D conductive structures can be well maintained during Li plating/stripping and hold a great potential for long cycle stability.

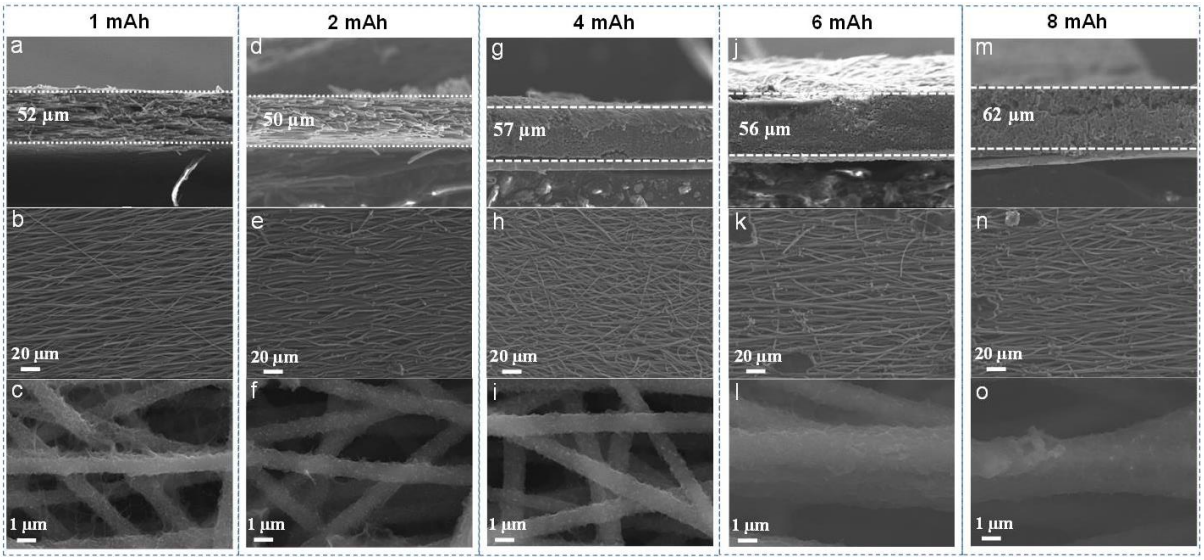

Figure 3. SEM images of Li@Co50 HCNF composite anodes: (a) Cross-sectional and (b,c) surface SEM images with initial plating 1 mAh cm^{-2}; (d) Cross-sectional and (e,f) surface SEM images with initial plating 2 mAh cm^{-2}; (g) Cross-sectional and (h,i) surface SEM images with initial plating 4 mAh cm^{-2}; (j) Cross-sectional and (k,l) surface SEM images with initial plating 6 mAh cm^{-2}; (m) Cross-sectional and (n,o) surface SEM images with initial plating 8 mAh cm^{-2}.

To evaluate the cycling performance of the Co based HCNF anodes, cyclic Li plating/stripping tests in symmetric cells were performed at various current densities with a fixed capacity of 0.5 mAh cm^{-2}. Figure 4a shows the voltage profiles of the Li@Co50 HCNF and Li@Cu at 2 mA cm^{-2}. The Li@Co50 HCNF has a low overpotential of $\approx$19 mV and cycles for >200 cycles. The enlarged figures on the right show their detailed voltage profiles. In contrast, the Li@Cu shows much larger overpotential with large fluctuations followed by an abrupt drop and finally failure with an internal short circuit after 155 cycles. A similar voltage profile can be seen in Figure 4b, where the Li@Co50 HCNF possesses stable cycling behaviour and has a low overpotential of $\approx$27 mV at 4 mA cm^{-2} for 0.5 mA h cm^{-2}, while the Cu foil shows a short-circuit after 150 cycles under the same conditions.

This improvement can be attributed principally to the 3D conductive networks and increased surface area of the Co50 HCNFs. As can be seen in Figure S2, Co50 has more hairs than the Co40, indicating that the Co50 can achieve better performance than the Co40 because of its increased surface area. To further prove this, the voltage profiles during Li plating/stripping on symmetrical cells were collected using bare Li foil (Figure S6a), a Li@Co40 HCNF anode (Figure S6b) and a Li@Co50 HCNF anode (Figure S6c) with a current density of 4 mA cm^{-2} with a fixed capacity of 0.5 mAh cm^{-2}. Here, Co50 has more

active sides to catch Li ions because of its relatively enhanced surface area and the porous micro structure which can provide a “cage” for the aimless Li ion. Therefore, the Co50 possesses better stability than the Co40 during Li plating/stripping cycles.

The Co50 HCNF exhibits a high and stable Coulombic efficiency over 99% for 140 cycles while this drops to below 58% after 100 cycles on the Cu foil current collector with a cycling capacity of 3 mAh cm^{-2} at a current density of 1 mA cm^{-2} (Figure 4c). In comparison, Figures 4d and 4e and Figure S7 show the charge-discharge curves of the Co50 and Cu foil with plating at 3 mAh cm^{-2} and a current density of 1 mA cm^{-2}. Figure 4d shows their initial first cycle Li deposition on the 3D Co50 host with a cycling capacity of 3 mAh cm^{-2} at a current density of 1 mA cm^{-2}, delivering negligible nucleation overpotential compared to that on bare Cu foil. The smaller values of the flat plating voltage plateaus of the Co50 based cells highlight the enhanced kinetics of Li deposition/stripping and smaller interfacial resistance because the enhanced mass transfer of the porous and conductive scaffolds. Therefore, the stable cycling performance with high Coulombic efficiency for the Co50 could be attributed to not only the connected 3D conductive structure but also the Co, O, and N-containing functional groups which can reduce the Li nucleation overpotential and guide an evenly distributed Li nucleation and growth on the surface of Co50 host.

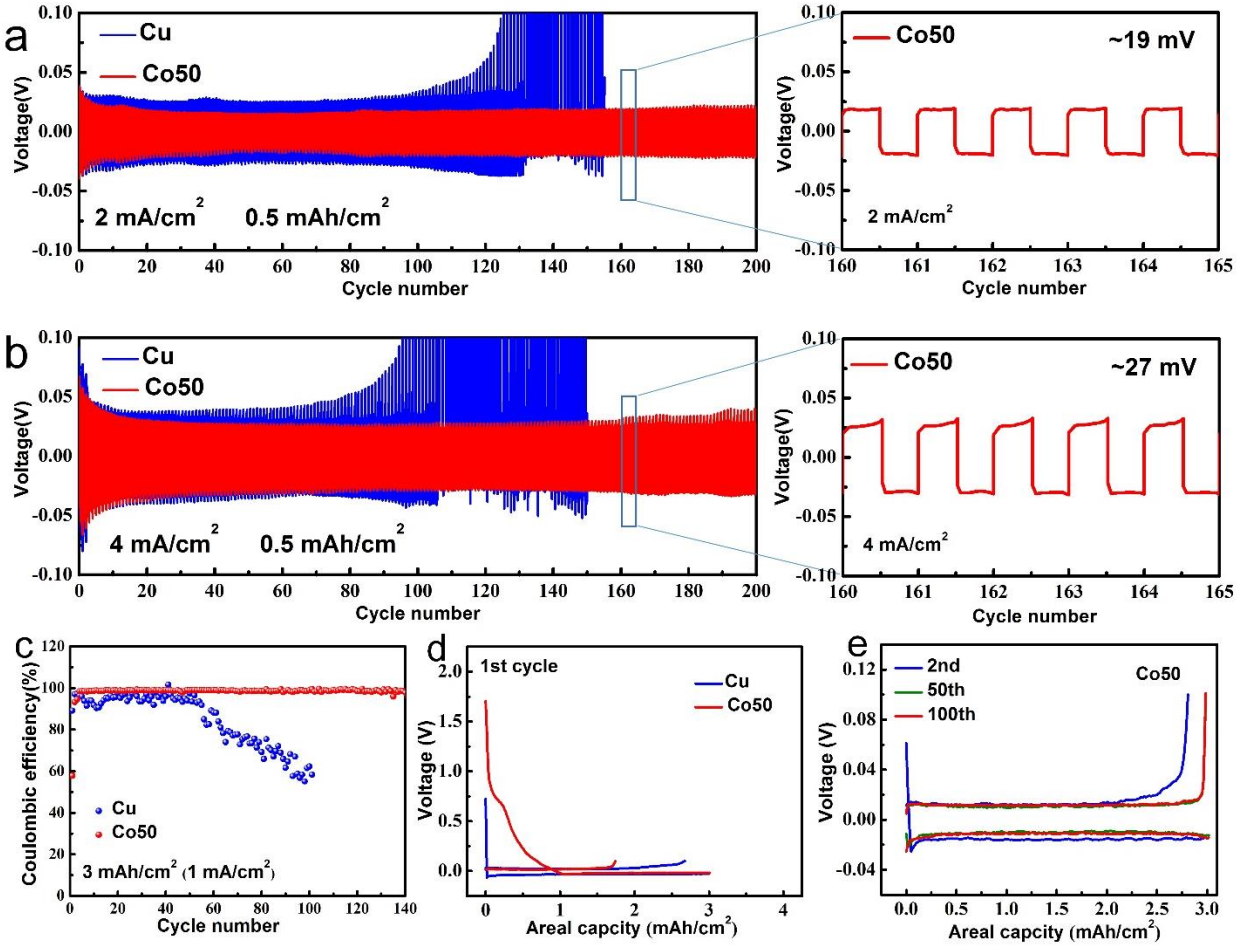

Figure 4. Voltage profiles of Li plating/stripping on symmetrical cells using bare Li foil (blue) and Li@Co50 HCNF composite anode (red) under current densities of (a) 2 mA cm−2 and (b) 4 mA cm−2 with a fixed capacity of 0.5 mAh cm−2. Enlarged figures on the right are detailed voltage profiles with cycle time indicated. Performance comparison of symmetrical cells using Co50 HCNF host and bare Cu foil with a cycling capacity of 3 mAh cm^{-2} at a current density of 1 mA cm^{-2}: The comparison of Coulombic efficiency (c) and voltage profiles of their 1st cycle (d); voltage profiles of the 2nd, 50th and 100th cycles for Co50 HCNF

anode (e). Performance comparison of symmetrical cells using Co50 HCNF host and bare Cu foil with a cycling capacity of 4 mAh cm^{-2} at a current density of 2 mA cm^{-2}.

The volume changes during the Li stripping/plating process have been regarded as another key issue that leads to rapid capacity decay and poor battery cycling stability. To further understand the effect of Li capacity utilization, the cycled Li metal anodes were extracted from the cells, and their morphologies were observed by using SEM after 100 cycles. Figure 5 shows that the hierarchical 3D anode can effectivily supress the formation of Li dendrites at various current densities. As shown in Figures 5d and 5e, the Li@Co50 HCNF anode has a uniform and smooth surface without metallic Li dendrite after 100 cycles of plating/stripping at 2 mA cm^{-2}. Similar results can be observed when the Li@Co50 HCNF anode experiences 100 cycles of plating/stripping at 4 mA cm^{-2} (Figures 5j and 5k) However, there is mossy and obvious Li dendrites on the surface of bare Li foil.

When the operating current density was increased from 2 mA cm^{-2} (Figures 5a-c) to 4 mA cm^{-2} (Figures 5g-i), the bare Li anode suffers from serious loosely stacked Li dendrites after 100 cycles of plating/stripping. Boulder-like mophologies and even cracks can be observed on the bare Li anode surface because of the limited nucleation sites of the Cu foil. Isolated Li nucleation sites can be seen after 100 cycles with 2 mA cm^{-2} in Figure 5a. When cycling at a higher current density of 4 mA cm^{-2}, the Li clumps grew and branch-like Li dendrite can be generated, suggesting the plating of Li was prone to deposit onto the Li clusters. Worse still, the coventional anode cannot maintain the volume changes during stripping/plating of metallic Li, thus leading to broken structures of Li on the surface of the bare Li foil. Figures 5f and 5l show the uniform thickness and very well maintained porous structures of the Co50 HCNF anode, indicating stable cycling because the 3D hierarchical conductive structure can completely accommodate the Li volume variations during repeated Li stripping/plating cycling. It can therefore be shown that the designed 3D hierarchical micostructures with increased surface area has favorable redox kinetics and reduces the plating/stripping charge transfer process.

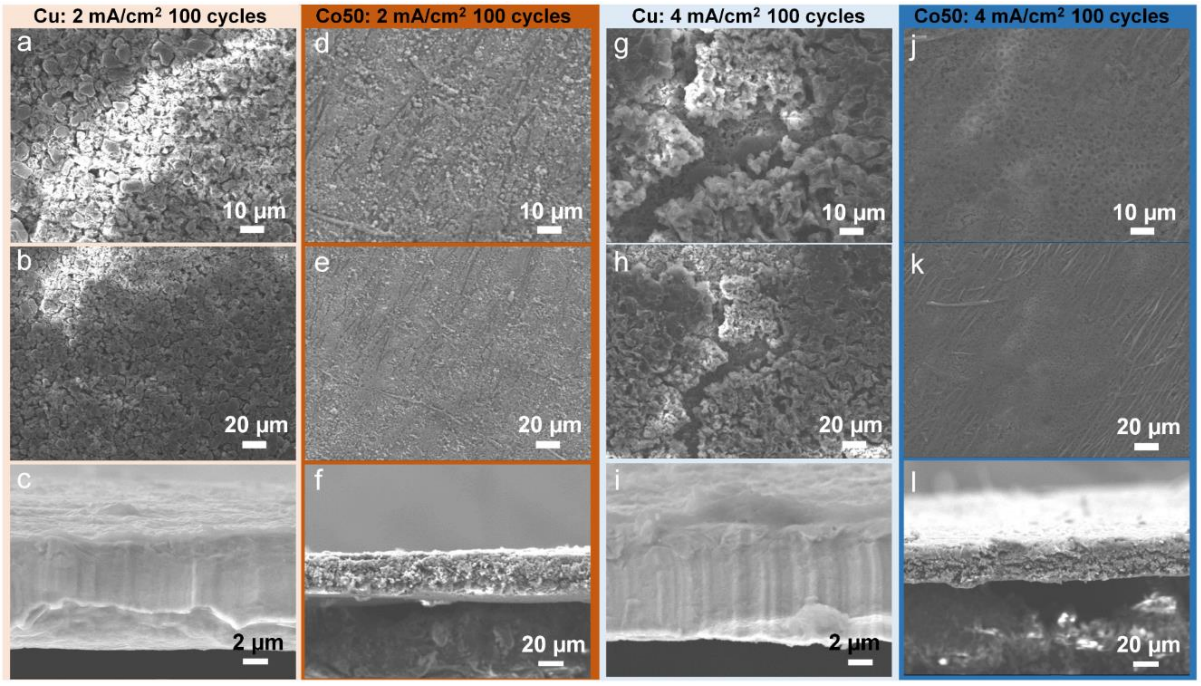

Figure 5. (a,b) SEM images of bare Li foil surface after 100 cycles of plating/stripping 2 mA cm^{-2}; (c) Cross-sectional SEM image of bare Li foil after 100 cycles of plating/stripping 2 mA cm^{-2}. (d,e) SEM images of Co50 HCNF host surface after 100 cycles of plating/stripping 2

mA cm^{-2}; (f) Cross-sectional SEM image of Co50 HCNF host after 100 cycles of plating/stripping 2 mA cm^{-2}. (g,h) SEM images of bare Li foil surface after 100 cycles of plating/stripping 4 mA cm^{-2}; (i) Cross-sectional SEM image of bare Li foil after 100 cycles of plating/stripping 4 mA cm^{-2}. (j,k) SEM images of Co50 HCNF host surface after 100 cycles of plating/stripping 4 mA cm^{-2}; (l) Cross-sectional SEM image of Co50 HCNF host after 100 cycles of plating/stripping 4 mA cm^{-2}.

The as-prepared Co50 HCNFs achieved excellent performance in half cells, and further full cells were fabricated by using Li@Cu and Li@Co50 HCNF as anodes paired with $LiNi_{0.5}Co_{0.2}Mn_{0.3}O_2$ (NCM_{523}) cathodes. Both Li@Cu and Li@Co50 HCNF anodes were plated with 8 mAh cm^{-2} Li. Their cycling and rate performance were tested to verify the performance of the advanced hairy carbon nanofibers for practical applications.

As can be seen from Figure 6d, the specific capacities of the Li@Co50 are higher than the Li@Cu one at a 1C cycling rate, and obvious difference in capacities can be observed especially when applying higher current densities. Thus, the Li@Co50/NCM cell can achieve much better rate capability than the cell with Li@Cu/NCM. The Li@Co50/NCM full cell achieves higher capacities of $\approx$111 mAh g^{-1} and $\approx$90 mAh g^{-1} at 5C and 10C, with the capacity showing much better stability, whereas the capacities for the Li@Cu/NCM full cell can only offer capacities of $\approx$99 mAh g^{-1} and $\approx$71 mAh g^{-1} at 5C and 10C, respectively. This can be attributed to the lower overpotential as shown in Figures 6a-6c, where the Li@Co50/NCM full cell shows lower overpotential in each charging plateau at 1C, 5C and 10C, thus indicating the significant enhancement in kinetic processes over the bare Li@Cu/NMC. The long-term cycling behaviours of the two cells are presented in Figure 6e. The Li@Co50/NCM full cell can deliver better stability and with a high Coulombic efficiency of $\approx$ 99.5% over 300 cycles at 5C without obvious capacity decay. However, the Li@Cu/NMC full cell suffered serious capacity decay after 200 cycles. These results further indicate excellent rate performance and cycling stability of the Co50 based cells, proving the material design principles and highlighting the great potential of the material for practical application.

Here, the designed 3D conductive structures and the functional groups can both contribute to the excellent battery performance. However, to the best of our knowledge, the effect of nanoparticle encapsulation in carbon is rarely explored. To better understand the superior battery performance of the Co-based hairy fibers, theoretical calculations based upon density function theory (DFT) were performed. Since Co exists on both the surface and the inside of the hairy fiber, the interaction of the Li atom on the cobalt, graphene and graphene (Co-based) surfaces is considered respectively. There are three typical adsorption sites on the Co(111) and graphene surfaces, i.e., bridge (B), hollow (H) and top (T) sites, as shown in Figure S8. According to the calculations, the adsorption energies between Li and graphene are -0.62 eV, -0.94 eV, and -0.61 eV, respectively, which are in good consistency with the values calculated by Chan et al.[25] (The adsorption energies of the hollow, bridge and top sites of graphene are -1.096, -0.773, and -0.754 eV, respectively). Table S1 lists the adsorption energies of the Li atom at the most stable sites. On Co(111), graphene and graphene (Co-based) surfaces, the Li atom prefers the hollow site with an adsorption energy of -2.80 eV, -0.94 and -1.67 eV, respectively. This suggests that the Li atom is adsorbed on Co(111) and graphene (Co-based) surfaces more easily compared to neat graphene surfaces. Based on the calculations, it is therefore concluded that the superior battery performance of the Co-based hairy fibers originate from the strong interaction between Li and Co and graphene with Co inside the hairs. Therefore, the CNTs with Co inside favour the easy and uniform Li deposition on the surface of the designed materials.

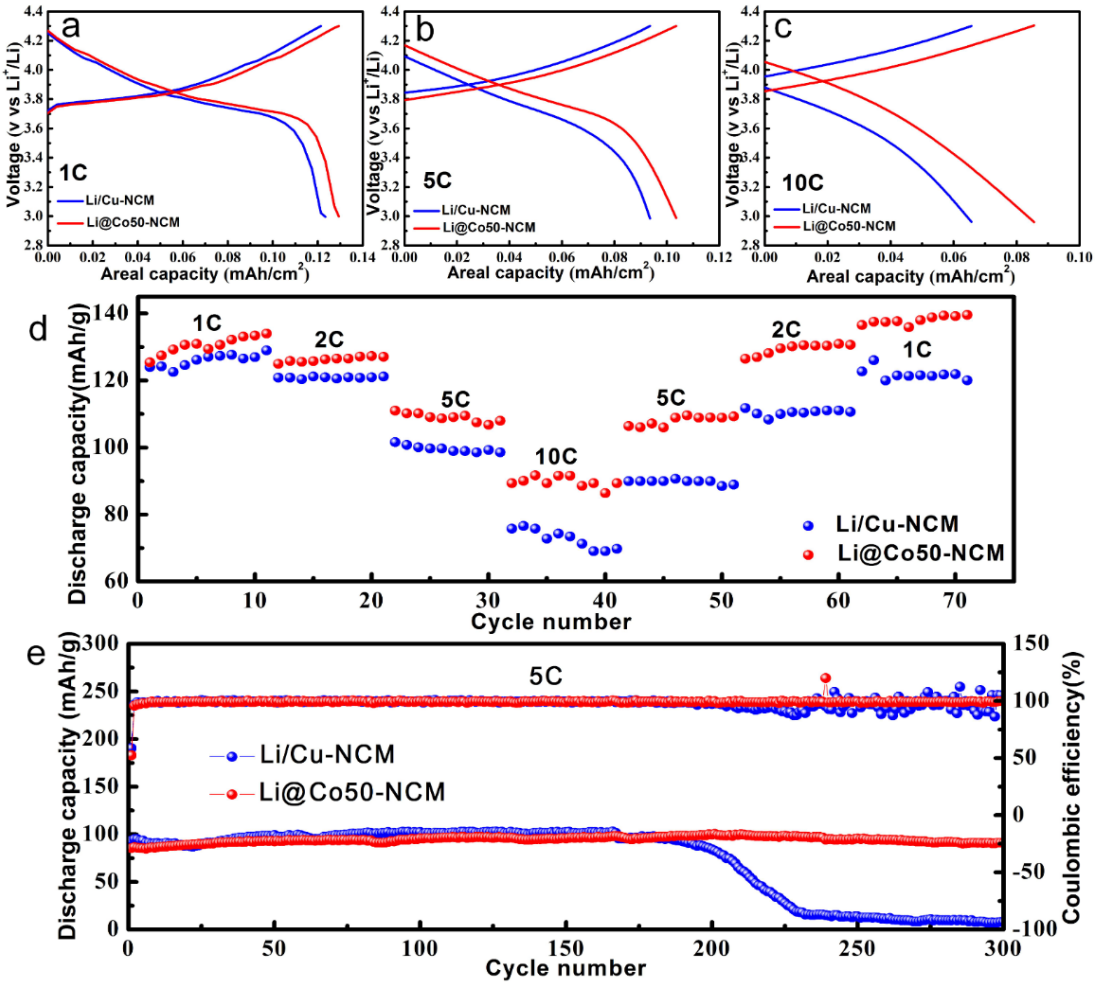

Figure 6. Electrochemical performance of the Li@Co50 HCNF and bare Li–Cu/NCM full cells. Voltage profiles for Li@Co50 HCNF and bare Li–Cu/NCM full cells under: a) 1 C, b) 5 C, and c) 10 C (1 C = 155 mA g^{-1}). d) Rate performance of Li@Co50 HCNF/NCM and bare Li–Cu/NCM full cells from 1 to 10 C. e) Cycling performance of Li@Co50 HCNF/NCM and bare Li–Cu/NCM full cells at 5 C over 300 cycles.

In conclusion, these remarkable properties and the performance of the hierarchical Co50 HCNFs can therefore be ascribed to the following reasons: (1) the conductive framework of the HCNFs with increased surface area can reduce the local current density and promote uniform Li deposition; (2) the highly conductive surface could decrease the overpotentional and improve the Coulombic efficiency; (3) the Oxygen and N-doped carbon host can provide strong interaction with Li atoms and resulting easy and uniform Li nucleation; (4) the Co particles and graphic carbon layer with Co inside also have strong interaction with Li, leading to more active sites for the Li nucleation and uniform deposition on the surface; (5) the free-standing 3D porous host can provide open pores to accommodate the volume variations during Li plating/stripping as well as mass transport routes for the Li-ions; (6) the continuous and conductive frame work can provide good mechanical strength and maintain constant electrode volume; (7) more importantly, electrospinning was employed as a facile and cost-effective approach to produce 3D porous conductive Co based carbon nanofibers for promoting evenly distributed Li, supressing Li dendrites and stabilizing the cycling performances, accelerating their practical application.

Experimental Section

An extensive description of material synthesis and characterization, device fabrication, and computational studies can be found in the Supporting Information.

Supporting Information

Supporting Information is available from the Wiley Online Library or from the author.

Conflict of Interest

The authors declare no conflict of interest.

*Email address: yangshichun@buaa.edu.cn

Acknowledgements

This work was kindly supported by the National Natural Science Foundation of China (No. U1864213), the EPSRC Joint UK-India Clean Energy Centre (JUICE) (EP/P003605/1), the EPSRC Multi-Scale Modelling project (EP/S003053/1), and the Innovate UK for Advanced Battery Lifetime Extension (ABLE) project. HW would like to thank the EPSRC for funding under EP/S000933/1.

Keywords

Li metal anode; mixed conductor interface; 3D porous host; dendrite free; metal-carbon nanofibers

[1] E. Environ, **2014**, 513.

[2] H. Wang, D. Lin, J. Xie, Y. Liu, H. Chen, Y. Li, J. Xu, G. Zhou, Z. Zhang, A. Pei, Y. Zhu, K. Liu, K. Wang, Y. Cui, **2019**, *1802720*, 1.

[3] R. Article, **2013**, 9011.

[4] E. Peled, S. Menkin, **2017**, *164*, DOI 10.1149/2.1441707jes.

[5] C. Yan, X. Cheng, Y. Tian, X. Chen, X. Zhang, W. Li, **2018**, *1707629*, 1.

[6] Y. Liu, D. Lin, P. Y. Yuen, K. Liu, J. Xie, R. H. Dauskardt, **2017**, 1.

[7] X. Zhang, X. Chen, R. Xu, X. Cheng, H. Peng, R. Zhang, J. Huang, Q. Zhang, **2017**, 14207.

[8] N. Li, Y. Shi, Y. Yin, X. Zeng, J. Li, C. Li, L. Wan, **2018**, 1505.

[9] Y. Gao, Z. Yan, J. L. Gray, X. He, D. Wang, T. Chen, Q. Huang, Y. C. Li, H. Wang, S. H. Kim, T. E. Mallouk, D. Wang, *Nat. Mater.* **2019**, *18*, DOI 10.1038/s41563-019-0305-8.

[10] C. Zhao, P. Chen, R. Zhang, X. Chen, B. Li, X. Zhang, **2018**, 1.

[11] R. Xu, X. Zhang, X. Cheng, H. Peng, C. Zhao, C. Yan, **2018**, *1705838*, 1.

[12] J. Xie, J. Wang, H. R. Lee, K. Yan, Y. Li, F. Shi, W. Huang, A. Pei, G. Chen, R. Subbaraman, J. Christensen, Y. Cui, **2018**, 2.

[13] R. Zhang, X. Shen, X. Cheng, Q. Zhang, *Energy Storage Mater.* **2019**, DOI

10.1016/j.ensm.2019.03.029.

[14] K. Liu, B. Kong, W. Liu, D. Lin, A. Pei, Y. Cui, K. Liu, B. Kong, W. Liu, Y. Sun, M. Song, J. Chen, Y. Liu, *Joule* **n.d.**, *2*, 1857.

[15] G. Huang, J. Han, F. Zhang, Z. Wang, H. Kashani, K. Watanabe, M. Chen, **2019**, *1805334*, 1.

[16] J. Xie, J. Ye, F. Pan, X. Sun, K. Ni, H. Yuan, X. Wang, N. Shu, C. Chen, Y. Zhu, **2019**, *1805654*, 1.

[17] F. Zhou, Z. Li, Y. Lu, B. Shen, Y. Guan, X. Wang, Y. Yin, B. Zhu, L. Lu, Y. Ni, Y. Cui, H. Yao, S. Yu, *Nat. Commun.* **2019**, 1.

[18] P. Xue, S. Liu, X. Shi, C. Sun, C. Lai, Y. Zhou, D. Sui, Y. Chen, J. Liang, **2018**, *1804165*, 1.

[19] L. Liu, Y. Yin, J. Li, S. Wang, Y. Guo, L. Wan, **2018**, *1706216*, 1.

[20] H. Kang, S. Woo, J. Kim, J. Yu, S. Lee, Y. Kim, **2016**, DOI 10.1021/acsami.6b09757.

[21] T. Zuo, X. Wu, C. Yang, Y. Yin, H. Ye, N. Li, **2017**, *1700389*, 1.

[22] D. Lin, Y. Liu, Z. Liang, H. Lee, J. Sun, H. Wang, K. Yan, J. Xie, Y. Cui, *Nat. Nanotechnol.* **2016**, *11*, 626.

[23] Y. Li, M. Afzaal, P. O'Brien, *J. Mater. Chem.* **2006**, *16*, 2175.

[24] F. Shi, Z. Geng, K. Huang, Q. Liang, Y. Zhang, Y. Sun, **2018**, *1800575*, DOI 10.1002/advs.201800575.

[25] K. T. Chan, J. B. Neaton, M. L. Cohen, **2008**, 1.